M101: Spectral Observations of H II Regions and Their Physical Properties

Ning Hu[1,2] , Enci Wang[1,2] , Zesen Lin[1,2] , Xu Kong[1,2] , Fuzhen Cheng[1,2], Zou Fan[3], Guangwen Fang[4], Lin Lin[5],
Yewei Mao[6], Jing Wang[7] , Xu Zhou[8], Zhiming Zhou[8], Yinan Zhu[3], and Hu Zou[8]

[1] CAS Key Laboratory for Research in Galaxies and Cosmology, Department of Astronomy,
University of Science and Technology of China, Hefei 230026, People's Republic of China
[2] School of Astronomy and Space Sciences, University of Science and Technology of China, Hefei 230026, People's Republic of China; huning@mail.ustc.edu.cn
[3] Key Laboratory of Optical Astronomy, National Astronomical Observatories, Chinese Academy of Sciences,
20A Datun Road, Chaoyang District, Beijing 100012, People's Republic of China
[4] Institute for Astronomy and History of Science and Technology, Dali University, Dali 671003, People's Republic of China
[5] Shanghai Astronomical Observatory, Chinese Academy of Science, 80 Nandan Road, Shanghai, 200030, People's Republic of China
[6] Purple Mountain Observatory, Chinese Academy of Sciences, Nanjing 210008, People's Republic of China
[7] CSIRO Astronomy and Space Science, Australia Telescope National Facility, P.O. Box 76, Epping, NSW 1710, Australia
[8] Key Laboratory of Optical Astronomy, National Astronomical Observatories, Chinese Academy of Sciences, Beijing 100012, People's Republic of China

Abstract

By using the Hectospec 6.5 m Multiple Mirror Telescope and the 2.16 m telescope of the National Astronomical Observatories, of the Chinese Academy of Sciences, we obtained 188 high signal-to-noise ratio spectra of H II regions in the nearby galaxy M101, which is the largest spectroscopic sample of H II regions for this galaxy so far. These spectra cover a wide range of regions on M101, which enables us to analyze two-dimensional distributions of its physical properties. The physical parameters are derived from emission lines or stellar continua, including stellar population age, electron temperature, oxygen abundance, etc. The oxygen abundances are derived using two empirical methods based on O3N2 and R_{23} indicators, as well as the direct T_e method when [O III] $\lambda 4363$ is available. By applying the harmonic decomposition analysis to the velocity field, we obtained a line-of-sight rotation velocity of 71 km s^{-1} and a position angle of 36°. The stellar age profile shows an old stellar population in the galaxy center and a relatively young stellar population in outer regions, suggesting an old bulge and a young disk. The oxygen abundance profile exhibits a clear break at ~18 kpc, with a gradient of -0.0364 dex kpc^{-1} in the inner region and -0.00686 dex kpc^{-1} in the outer region. Our results agree with the "inside-out" disk growth scenario of M101.

Key words: galaxies: evolution – galaxies: fundamental parameters – galaxies: individual (M101) –
galaxies: stellar content

1. Introduction

H II regions are sites of strong star formation in galaxies, which make H II regions perfect probes of star formation processes, evolution of massive stars, and the surrounding interstellar medium. Plenty of information can be obtained by analyzing the emission lines and underlying stellar continuum of their spectra. The gas-phase metallicity, defined as the number ratio of oxygen to hydrogen atoms, is one of the key properties in galaxy formation and evolution. The oxygen is synthesized in high-mass stars ($>8\ M_\odot$) and then released to the interstellar medium through stellar winds or supernova explosion. The spatial distributions of the oxygen abundance in galaxies are affected by a variety of processes, such as enriched outflows (Tremonti et al. 2004), accretion (Dalcanton et al. 2004), and mergers (Kewley et al. 2006, 2010; Rupke et al. 2010; Rich et al. 2012; Torrey et al. 2012; Sánchez et al. 2014). Thus studying the metallicity and its relation with other properties would provide clues on the galaxy formation and evolution.

Research on the metallicity of H II regions has been booming in the last two decades. Zaritsky et al. (1994) and van Zee et al. (1998) found that H II regions have an average metallicity gradient of -0.05 dex kpc^{-1}, i.e., the inner regions of galaxies are more metal-rich than the outskirts. The negative gradients are found to be universal, as reviewed by many (such as Bresolin 2007; Li et al. 2013; Scarano & Lépine 2013; Sánchez et al. 2014; Ho et al. 2015; Sánchez-Menguiano et al. 2016),

suggesting inner-to-out transportation of metals. Observations also show breaks in the oxygen abundance gradients in a number of galaxies (Zaritsky 1992; Roy & Walsh 1997). Pilyugin (2003) claimed that such breaks are due to the systematic error involving the excitation parameter, while others attribute it to the barrier effect of corotation, which isolates the inner and outer regions of one disk from the other due to opposite directions of gas flow (Lépine et al. 2011; Scarano & Lépine 2013). More recently, several studies focusing on gas content have found that the metallicity gradients flatten to a constant value beyond the isophotal radii R_{25} or $2R_e$ (Rosales-Ortega et al. 2011; Marino et al. 2012; Sánchez et al. 2012b, 2014; López-Sánchez et al. 2015; Sánchez-Menguiano et al. 2016), and several scenarios are proposed to explain the nature of this flattening, such as the bar-induced radial gas flows (Cavichia et al. 2014), minor mergers, and perturbations from satellite galaxies (Bird et al. 2012; López-Sánchez et al. 2015), the varying of star formation efficiency over large galactocentric distances (Bresolin et al. 2012; Esteban et al. 2013), and the balance between outflows and inflows with the intergalactic medium (Oppenheimer & Davé 2008; Oppenheimer et al. 2010; Davé et al. 2011, 2012).

Recently, the integral field unit (IFU) spectrograph has become an important and powerful tool for spatial-resolved spectroscopic observations, which has greatly increased the progress of the two-dimensional research on galaxies. Many surveys, using IFU technology, have been carried out, such as

SAURON (Bacon et al. 2001), PINGS (Rosales-Ortega et al. 2010), CALIFA (Sánchez et al. 2012a), and MaNGA (Bundy et al. 2015). According to their different observational strategies, MaNGA is mapping a large number of galaxies with limited spatial resolution (1–3 kpc) and field of view (~70 acrsec), while PIGNS provides a better spatial resolution and larger field of view but with a limited number of galaxies, and CALIFA is a compromise between the two. Sánchez et al. (2014) found a common metallicity gradient of -0.10 ± 0.09 dex R_e^{-1} for 193 CALIFA galaxies, and the metallicity gradients do not exhibit the dependence on other properties of galaxies, such as morphology, mass, and the presence or absence of bars (Sánchez-Menguiano et al. 2016). By studying 49 local field star-forming galaxies, Ho et al. (2015) proposed a local benchmark of metallicity gradients of -0.39 ± 0.18 dex R_{25}^{-1}. More recently, Belfiore et al. (2017) analyzed 550 nearby galaxies from the MaNGA survey and confirmed that the metallicity gradient is flat for low-mass galaxies ($M_* < 10^{9.0}\,M_\odot$), steepens for more massive galaxies until $M_* \sim 10^{10.5}\,M_\odot$, and flattens lightly again for even more massive galaxies. This research provided strong constraints on the galactic chemical composition of nearby galaxies (Chiappini et al. 2001; Fu et al. 2009; Ho et al. 2015; Sánchez-Menguiano et al. 2016; Belfiore et al. 2017).

Kong et al. (2014) proposed the "Spectroscopic Observations of the H II Regions In Nearby Galaxies (H2ING)" Project, which has performed spectroscopic observations on H II regions in 20 nearby large galaxies since 2008. As the third paper of this project, we report the spectroscopic observation of H II regions in nearby galaxy M101, with the Multiple Mirror Telescope (MMT) 6.5 m telescope (Fabricant et al. 2005) and the National Astronomical Observatories, Chinese Academy of Sciences (NAOC) 2.16 m telescope (Fan et al. 2016). M101 (also known as NGC 5457, $\alpha = 14^h03^m12^s.5$, $\delta = +54°20'56''$) is a large face-on Scd galaxy containing plenty of H II regions (Hodge et al. 1990; Kennicutt et al. 2003; Bresolin 2007; Gordon et al. 2008; Croxall et al. 2016). It has a distance of about 7.4 Mpc and an apparent scale of about 36 pc arcsec^{-1}, which enables us to observe its H II regions to a scale of a few hundred parsecs with our 1''5 fiber and 2''5 slit observations. A major-axis position angle of 39° and an inclination angle of 18° (Bosma et al. 1981) allow us to perform detailed studies of its stellar populations and ionized nebulae. Observations of the M101 H II regions have been carried out since the 1970s (Searle 1971; Smith 1975; McCall et al. 1985; Kennicutt & Garnett 1996; Bresolin 2007). Recently, Li et al. (2013) presented a catalog containing 79 H II regions from their observations and several previous works since 1996. Croxall et al. (2016) have enlarged the sample of H II regions by using the Large Binocular Telescope, and obtained 109 spectra of H II regions in M101. In this paper, we have obtained 188 H II regions with high signal-to-noise ratios (S/Ns) from our observations, which is the largest spectroscopic sample of H II regions for M101.

With the spectra of numerous H II regions, we have derived the physical properties of H II regions, and presented a detailed study of the spatial distribution of these properties. This paper is structured as follows. In Section 2, we describe the observation, data reduction and emission line measurements. In Section 3, we present the measurements and analysis of physical properties of the H II region sample. Metallicities are derived with three methods and the gradient is also calculated and discussed. We summarize our results in Section 4.

2. Data

2.1. Observations

The H II region candidates are selected from the continuum-subtracted Hα image (Hoopes et al. 2001). Candidates are primarily selected with a preference for large regions, using SExtractor (Bertin & Arnouts 1996) with the irregular area filter with at least 25 pixels (1 pixel = 2''028). The foreground stars are excluded from the H II catalog by matching with the 2MASS all-sky Point Source Catalog (Cutri et al. 2003). Then candidates are observed with the Hectospec multi-fiber positioner and spectrograph on the 6.5 m MMT telescope and the NAOC 2.16 m telescope.

The usable field of the MMT 6.5 m telescope is 1° in diameter, and the instrument deployed three hundred 1''5-diameter fibers on the field, corresponding to ~54 pc at the distance of M101. We used Hectospecs 270 gpm grating that provided a dispersion of 1.2 Å pixel^{-1} and a resolution of ~5 Å. The spectral wavelength coverage is from 3650 to 9200 Å. The Hectospec fiber assignment software *xfitfibs*[9] allows the user to assign rankings to targets. If we ignored the spatial positions of our targets, fiber collisions would prevent many objects in the center portion of the center of M101 from being observed. We therefore assigned priority to H II regions based on their Hα fluxes. We observed two fields on the night of 2012 February 10 with 3600 s exposure times and one field on 2013 March 15 with 5400 s exposure times. Weather conditions are clear on both nights, and seeings are about 1''2, 0''8 and 0''6 for each field, respectively.

The NAOC 2.16 m telescope worked with an OMR (Optomechanics Research Inc.) spectrograph providing a dispersion of 4.8 Å pixel^{-1} and a resolution of 10 Å. The observed spectra cover the wavelength range of 3500–8100 Å. Slits of 2''5 are placed manually to cover as many candidates as possible and to avoid those observed by MMT. Observations are carried out over nine nights between 2012 and 2014 with 20 slits, and exposure times varied between 3600 and 5400 s depending on weather conditions. Typical seeing is ~2''5, corresponding to a spatial resolution of ~300 pc.

2.2. Data Reduction

2.2.1. MMT Spectra

We obtained over 300 spectra from MMT observations, and these spectra are reduced in a uniform manner with the publicly available HSRED[10] software. The frames are first debiased and flat-fielded. Individual spectra are then extracted and wavelength calibrated. Sky subtraction is achieved with Hectospec by averaging spectra from "blank sky" fibers from the same exposures. Three spectra of the same target are reduced and combined into one final spectrum. Standard stars are obtained intermittently and are used to calibrate spectra using the IRAF ONEDSPEC package. These relative flux corrections are carefully applied to ensure that the relative line flux ratios are accurate. We have checked the spectra through visual inspection to exclude spectra with problematic continuum

---

9 https://www.cfa.harvard.edu/mmti/hectospec/xfitfibs/
10 http://mmto.org/rcool/hsred/index.html
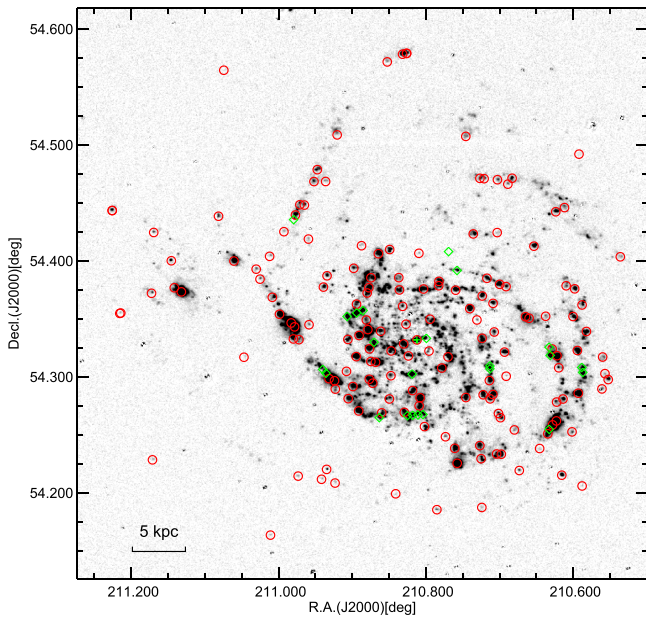
Figure 1. Locations of H II regions of the final 188 samples on the narrowband Hα image of M101 observed with KPNO Schmidt telescope (Hoopes et al. 2001). Two symbols represent spectra from two telescopes: red circles from MMT and green diamonds from NAOC. The green cross marks the center of the galaxy.

shape, or missing Hα and Hβ emission lines. Finally, we obtained a sample of 164 H II region spectra for analysis. The 164 spectra have a median S/N of 35 at 5000 Å, and over 50 spectra have S/Ns higher than 60.

2.2.2. NAOC 2.16 m Spectra

The spectroscopic data from NAOC 2.16 m observations are reduced following standard procedures using the IRAF software package. The CCD reduction includes bias and flat-field corrections, as well as cosmic-ray removal. Wavelength calibration is performed based on helium/argon lamps exposed at both the beginning and the end of each slit during the observation. Flux calibration is performed based on observations of the KPNO spectral standard stars (Massey et al. 1988) observed at the end of each slit observation. The atmospheric extinction is corrected by using the mean extinction coefficients measured for Xinglong by the Beijing–Arizona–Taiwan–Connecticut multicolor sky survey (H. J. Yan 1995, private communication). Similar to MMT spectra, those with problematic continuum shape or missing Hα and Hβ emission lines are excluded. Finally, we extracted 41 spectra, among which 17 spectra are also observed by the MMT 6.5 m telescope. Considering the higher S/Ns and better resolution of MMT spectra, we use MMT spectra for these 17 candidates, and NAOC observations provide 24 additional spectra.

Finally, we have 188 spectra in total (164 from MMT 6.5 m and 24 from NAOC 2.16 m). Locations of these H II regions are shown in Figure 1 and their coordinates are listed in Table 1. Velocities are measured using the SAO xcsao package with IRAF (see Figure 2). We have carefully checked the velocities and corrected a few bad results manually. Spectra are corrected for Galactic reddening (Schlegel et al. 1998) and then shifted to rest frame for further measurements.

2.3. Spectral Fitting

To measure the emission lines of each individual spectra, the underlying stellar continuum must be subtracted. We perform a modeling of stellar continuum using the advanced ICA algorithm, mean field approach to Bayesian independent component analysis (MF-ICA), which is comparatively precise and efficient (Højen-Sørensen et al. 2001, 2002). The MF-ICA approach extracts 12 independent components (ICs) from BC03[11] (Bruzual & Charlot 2003). The 12 ICs contain the full information of the BC03 library and excellently recover the library, which spans a stellar age range from 1.0×10^5 to 2.0×10^{10} year, and an initial chemical composition metallicity from 0.0001 to 0.1. The star formation histories are parameterized in terms of an underlying continuous model superimposed with random bursts on it (Kauffmann et al. 2003). The intrinsic starlight reddening is modeled by the extinction law of Charlot & Fall (2000). The velocity dispersion is set to vary between 50 and 450 km s^{-1}. MF-ICA provides reliable modeling of stellar continuum and estimates physical parameters accurately with a large improvement in efficiency. More detailed information about the MF-ICA algorithm is described in Hu et al. (2016). Figure 3 shows two typical fitting results. For each spectrum, emission lines [O II] λ3727, Hβ + [O III] λλ4959, 5007, Hα + [N II] λλ6548, 6583, and [S II] λλ6717, 6731 are enlarged in four small panels below the spectrum.

2.4. Line Flux Measurement

After subtracting the stellar continuum, we perform the nonlinear least-squares fit to emission lines using the MPFIT package implemented in IDL (Markwardt 2009). Each emission line is modeled with one Gaussian profile, and we constrain the ratios [N II] λ6583/[N II] λ6548 and [O III] λ4959/[O III] λ5007 to their theoretical values given by quantum mechanics. The emission line fluxes are measured by integration of the flux based on the fitted profiles.

The interstellar reddening is corrected by comparing the observed Hα/Hβ Balmer decrement to the theoretical value, since the intrinsic value of Hα/Hβ is not very sensitive to the physical conditions of the gas. Assuming Hα/Hβ = 2.86 and $R_V = 3.1$ with the Cardelli et al. (1989) extinction curve under the case-B recombination, the extinction in the V band is given by

$$A_V = 6.77 \log \frac{F(\text{H}\alpha)/F(\text{H}\beta)}{2.86}. \quad (1)$$

negative color excesses are all set to zero. The reddening-corrected line flux measurements are listed in Table 1, with values normalized to Hβ flux. All spectra have strong Hα and Hβ emission lines, and 14 of them have [O III] λ4363 emission line.

In Figure 4, we examine the excitation properties of our sample by plotting [O III] λ5007/Hβ versus [N II] λ6583/Hα diagnostic diagrams (BPT, Baldwin et al. 1981). The color-code indicates the deprojected distance to the galaxy center. We plot the boundaries between different photo-ionization sources (star-forming regions and active galactic nuclei) by Kewley et al. (2001) and Kauffmann et al. (2003). As shown in Figure 4, almost all targets in our

---
[11] http://www.bruzual.org

3

Table 1
Coordinates and Dereddened Line Fluxes of H II Regions in M101

| ID	R.A.	Decl.	[O II] λ3727	[Ne III] λ3869	Hδ λ4102	Hγ λ4340	[O III] λ4363	[O III] λ4959	[O III] λ5007	[He I] λ5876	[O I] λ6300	[N II] λ6548	Hα λ6563	[N II] λ6583	[S II] λ6717	[S II] λ6731	Hβ λ4861
1	14:03:01.15	54:14:27.0	276.4	19.5	26.5	48.1	82.44	99.4	294.7	10.9	6.5	9.9	285.9	28.4	22.4	16.5	3611.51
			0.6	0.2	0.1	0.3	0.09	0.01	0.8	0.03	0.04	0.07	1.1	0.1	0.11	0.09	12.85
2	14:02:44.66	54:23:36.1	344.0	...	30.2	51.6	...	43.7	128.5	8.9	...	15.6	228.7	44.6	20.3	14.3	3478.57
			0.2	...	0.1	0.2	...	0.09	0.2	0.1	...	0.06	0.6	0.1	0.11	0.09	7.04
3	14:02:49.49	54:17:42.5	294.0	...	28.3	48.1	...	49.7	148.8	11.3	...	19.0	286.0	54.4	35.0	24.1	276.81
			1.9	...	0.6	0.4	...	0.05	1.3	0.4	...	0.01	2.4	0.4	0.66	0.32	2.37
4	14:02:20.22	54:23:12.8	434.4	...	40.7	46.6	...	51.2	152.7	11.9	...	11.1	286.9	31.9	41.5	28.1	131.22
			5.0	...	1.2	3.5	...	0.07	1.2	0.6	...	0.02	1.9	0.9	0.95	0.92	2.77
5	14:02:20.65	54:17:48.9	389.9	27.1	26.2	46.4	23.73	94.7	283.2	10.3	8.1	8.9	275.3	25.6	29.3	21.3	510.45
			2.4	0.9	0.5	0.4	0.35	0.01	1.2	0.3	0.2	0.05	1.3	0.2	0.07	0.18	6.79
6	14:03:45.54	54:13:53.3	482.9	43.4	...	77.8	...	103.1	304.0	...	...	4.8	236.9	13.6	16.9	16.6	174.60
			3.3	1.3	...	1.8	...	0.09	1.0	...	...	0.01	0.8	0.4	0.51	0.24	1.69
7	14:03:41.73	54:19:4.0	374.0	21.2	36.3	56.6	...	94.3	275.3	9.6	3.9	10.5	286.0	29.9	14.1	11.2	23703.82
			0.1	0.01	0.02	0.1	...	0.04	0.2	0.01	0.1	0.02	0.4	0.02	0.03	0.02	24.11
8	14:03:34.05	54:18:37.1	174.1	12.1	30.0	50.7	...	86.3	256.0	12.6	2.6	11.9	252.0	34.0	9.1	7.5	18061.50
			0.3	0.1	0.2	0.3	...	0.6	0.6	0.1	0.1	0.01	1.2	0.1	0.04	0.05	63.28
9	14:02:46.64	54:14:49.7	334.0	40.9	29.5	56.4	7.29	125.1	374.6	8.6	12.7	15.9	286.0	45.5	44.6	32.2	354.90
			2.2	0.9	0.8	0.4	0.38	0.02	2.4	0.2	0.5	0.01	2.2	0.5	0.50	0.27	2.75
10	14:03:27.54	54:18:45.0	153.5	...	31.9	52.3	...	7.0	20.8	8.6	3.3	28.8	269.0	82.6	43.5	28.3	442.82
			1.2	...	0.5	0.5	...	0.01	0.4	0.2	0.2	0.01	0.9	0.5	0.51	0.25	1.80
11	14:02:29.51	54:16:14.1	295.0	15.8	25.6	46.4	...	92.9	275.6	10.9	6.6	10.7	251.7	30.7	26.3	18.0	1471.36
			0.8	0.2	0.3	0.4	...	0.01	0.5	0.1	0.2	0.02	1.0	0.2	0.12	0.15	6.10
12	14:02:46.97	54:16:56.1	280.2	...	33.0	36.7	...	21.6	64.7	...	8.8	26.1	286.0	74.9	40.1	23.5	110.45
			4.0	...	2.1	1.3	...	0.02	1.9	...	0.7	0.01	3.0	0.7	0.95	0.62	1.72
13	14:03:12.28	54:17:54.2	222.8	...	14.0	49.0	...	21.2	63.6	11.6	...	27.8	279.3	79.8	44.1	30.3	164.75
			2.8	...	0.8	2.2	...	0.01	1.6	0.6	...	0.03	1.6	0.8	1.06	0.22	2.31
14	14:02:20.29	54:20:1.4	275.7	21.6	28.6	47.3	...	100.1	300.4	11.0	6.2	7.0	286.2	20.2	18.6	13.5	576.54
			2.5	0.6	0.8	0.8	...	0.02	1.7	0.2	0.2	0.04	2.1	0.2	0.17	0.22	5.98
15	14:02:12.15	54:19:37.9	175.2	78.7	...	...	...	227.3	681.8	...	...	...	237.9	...	...	...	34.70
			11.6	6.4	...	...	...	0.04	6.5	...	...	...	2.3	...	...	...	1.69

Note. Line fluxes are normalized to Hβ line, after correcting for reddening. Hβ λ4861 is the measured Hβ flux in units of $\times 10^{-17}$ erg s^{-1} cm^{-2}, corrected for extinction.
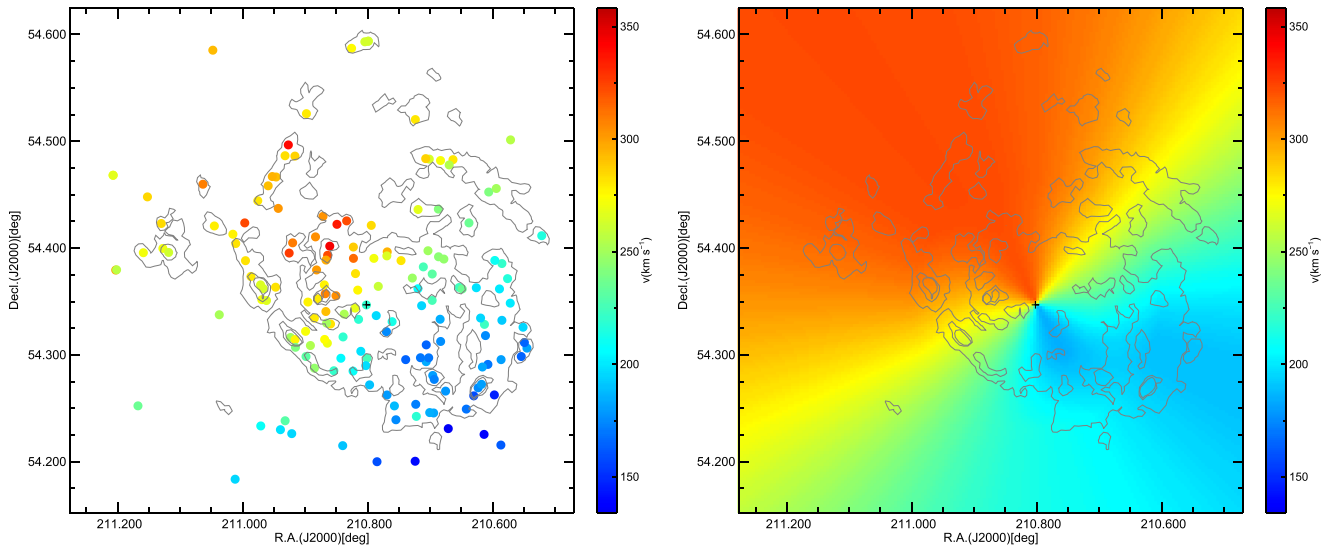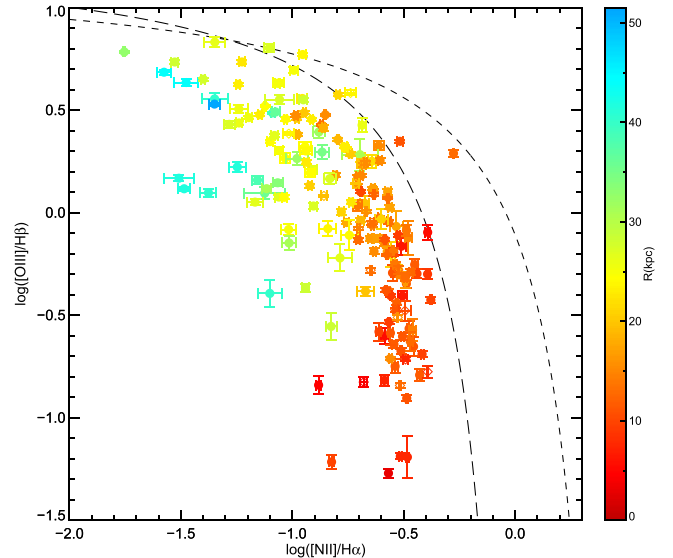
Figure 2. Velocity field of M101. Left: the line-of-sight velocities of H II regions. Right: modeled velocity map using the method from Krajnović et al. (2006). Contours show the shape of M101 in the Hα image, and the center of the galaxy is marked with a black cross.
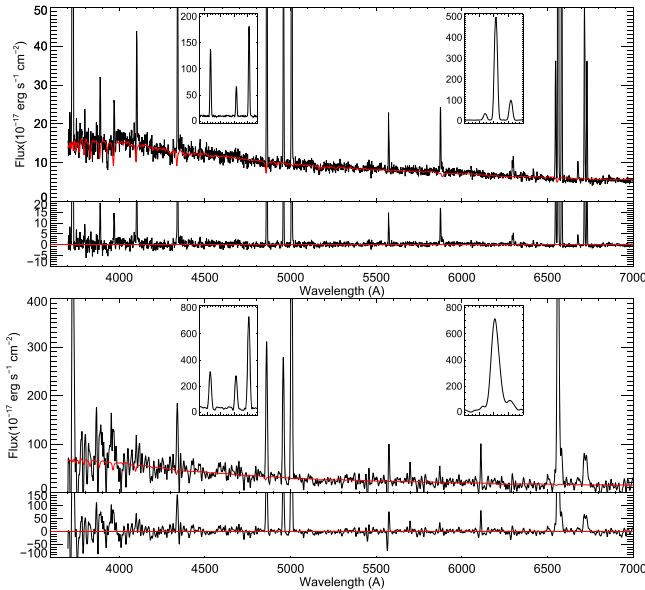
Figure 3. Typical spectrum of H II regions in M101 observed by MMT (upper panel) and NAOC 2.16 m (lower panel). Panels show the observed spectra (black line) and MF-ICA continuum fit (red line), and the two small insets of each spectrum zoom in on several strong emission lines: Hβ + [O III] λλ4959,5007, Hα + [N II] λλ6548, 6583.

Figure 4. BPT diagram showing the excitation properties of our H II regions. The boundaries are taken from Kewley et al. (2001, short-dashed line) and Kauffmann et al. (2003, long-dashed line). Filled points are from MMT and diamonds are from NAOC, and colors indicate the deprojected distance to the galaxy center. Almost all targets in our sample are located in the pure star-forming region of the diagram with a clear profile against the deprojected distances to the galaxy center.

sample are located in the pure star-forming region with only five exceptions. Furthermore, the H II regions show a radially changing sequence on the BPT diagram: the inner regions have higher [N II] λ6583/Hα and lower [O III] λ5007/Hβ than outer regions, suggesting a negative gradient of metallicity. This is consistent with the results from Sánchez et al. (2015) in which the inner H II regions of the galaxies appear to have higher [N II] λ6583/Hα and lower [O III] λ5007/Hβ than outer regions, using over 5000 H II regions from 306 galaxies.

More detailed information will be discussed in Section 3.3.

2.5. Oxygen Abundance Determination

2.5.1. The Direct Method

The direct method to derive oxygen abundance is to measure the ratio of a higher excitation line to a lower excitation line, in which case [O III]λ4363/[O III]λλ4959, 5007 is the most commonly used. This ratio together with a model of two excitation zone structure for the H II regions provides an estimation of the electron temperature of the gas, and then the electron temperatures are converted to oxygen abundances with corrections for an unseen stage of ionization.

Table 2
Gas Conditions and Oxygen Abundance Measurements

ID	T[O III] (K)	n_e (cm^{-3})	$\log q$ (log cm s^{-1})	12 + log(O/H)		
				O3N2	KK04	T_e
1	10120 ± 1134	76 ± 12	7.77 ± 0.153	8.27 ± 0.023	8.68 ± 0.009	8.32 ± 0.933
2	...	29 ± 7	7.47 ± 0.019	8.46 ± 0.013	8.83 ± 0.002	...
3	...	...	7.60 ± 0.654	8.45 ± 0.070	8.85 ± 0.009	...
4	...	...	7.37 ± 1.145	8.37 ± 0.096	8.68 ± 0.012	...
5	13696 ± 1415	62 ± 11	7.57 ± 0.388	8.25 ± 0.036	8.59 ± 0.017	7.94 ± 0.820
6	...	539 ± 30	7.55 ± 3.646	8.17 ± 0.036	8.63 ± 0.009	...
7	...	170 ± 29	7.58 ± 0.056	8.31 ± 0.006	8.60 ± 0.002	...
8	...	215 ± 37	8.05 ± 0.394	8.32 ± 0.021	8.85 ± 0.004	...
9	9519 ± 2096	53 ± 20	7.68 ± 0.343	8.29 ± 0.057	8.51 ± 0.020	8.52 ± 1.876
10	...	...	7.33 ± 0.773	8.78 ± 0.078	9.11 ± 0.003	...
11	...	...	7.72 ± 0.283	8.29 ± 0.017	8.69 ± 0.008	...
12	...	...	7.39 ± 1.443	8.61 ± 0.165	8.95 ± 0.010	...
13	...	...	7.53 ± 1.244	8.62 ± 0.147	9.02 ± 0.010	...
14	...	62 ± 15	7.65 ± 0.572	8.21 ± 0.050	8.47 ± 0.206	...
16	...	59 ± 16	...	...	9.16 ± 0.004	...
17	...	...	7.96 ± 1.300	8.45 ± 0.039	8.89 ± 0.008	...
18	15259 ± 764	69 ± 27	7.65 ± 0.539	8.20 ± 0.043	8.46 ± 0.133	7.79 ± 0.390
19	...	20 ± 7	...	...	9.03 ± 0.004	...
20	...	...	7.44 ± 2.586	8.57 ± 0.114	8.95 ± 0.018	...
21	...	113 ± 34	7.48 ± 0.211	8.68 ± 0.023	9.07 ± 0.002	...
22	...	...	7.76 ± 2.431	8.25 ± 0.088	8.61 ± 0.018	...
23	...	164 ± 35	...	...	...	...
24	...	25 ± 9	7.42 ± 0.569	8.59 ± 0.115	8.96 ± 0.011	...
25	...	...	7.69 ± 2.493	8.55 ± 0.101	9.02 ± 0.006	...
26	...	55 ± 12	7.43 ± 0.433	8.44 ± 0.038	8.68 ± 0.010	...
27	...	...	...	...	8.86 ± 0.013	...
28	...	498 ± 22	7.42 ± 0.453	8.29 ± 0.089	8.66 ± 0.024	...
29	...	923 ± 83	7.39 ± 0.445	8.30 ± 0.255	8.51 ± 0.179	...
30	...	182 ± 15	7.56 ± 3.270	8.33 ± 0.144	8.79 ± 0.014	...

To calculate the total oxygen abundances, we make the usual assumption: O/H = $(O^+ + O^{2+})/H^+$. Electron temperatures are derived based on the emission line intensity ratio [O III] $\lambda4363$/[O III] $\lambda\lambda4959, 5007$, and electron densities (n_e) are derived based on the intensity ratio [S II] $\lambda6717$/[S II] $\lambda6731$. Among the spectra of H II regions, 14 of them have [O III] $\lambda4363$ detections with well-defined line profiles and the S/Ns larger than 3. The electron temperatures of them for the O^{2+}-emitting region (T[O III]) are derived with the PYNEB package (Luridiana et al. 2015). PYNEB is a python package for analyzing emission lines, which includes the Fortran code FIVEL (De Robertis et al. 1987) and the IRAF nebular package (Shaw & Dufour 1995). We adopted the transition probabilities of Wiese et al. (1996) and Storey & Zeippen (2000) for O^{2+}, Podobedova et al. (2009) for S^+, the collision strengths of Aggarwal & Keenan (1999) for O^{2+}, Tayal & Zatsarinny (2010) for S^+. Electron temperatures and electron densities are calculated simultaneously to obtain self-consistent estimates by PYNEB. Then the electron temperatures of [O II] (T[O II]) are obtained with applying the relation from Garnett (1992): T[O II] = $0.7 \times T$[O III] + 3000 K. With giving T[O II], T[O III], and n_e, metallicities are finally calculated from the line intensities of [O II] $\lambda3727$ and [O III] $\lambda\lambda4959$, 5007 with PYNEB.

Errors are estimated with a Monte Carlo algorithm by repeating the calculation 2000 times. In each calculation, the input flux of each emission line is generated from a Gaussian distribution with the mean value equaling the measured emission line flux and the standard deviation equaling its error. We use the median value of 2000 results as the final value, and

half of the 16%–84% range of this distribution as the corresponding error. The electron temperatures and densities are listed in Table 2.

Although the direct method is considered to be one of the most reliable methods to derive gas-phase oxygen abundances, the [O III] $\lambda4363$ line is weak, especially in meta-rich environments. Since most of our H II regions do not have [O III] $\lambda4363$ detections, we applied two strong-line methods to determine the oxygen abundance.

2.5.2. The O3N2 Index

The O3N2 index, defined as O3N2 = log{([O III] $\lambda5007$/Hβ)/([N II] $\lambda6583$/Hα)}, was first introduced by Alloin et al. (1979). It is widely used to diagnose oxygen abundances in the literature. The four lines involved in the index are easily detected, and the close wavelength between the two pairs of lines make the index nearly free from extinction. By using 137 extragalactic H II regions, Pettini & Pagel (2004) empirically calibrated the O3N2 versus oxygen abundance determined by the T_e method and photoionization models. More recently, Marino et al. (2013) provide a new calibration with T_e based metallicities of 603 H II regions, which is adopted here:

$$12 + \log(O/H) = 8.533 - 0.214 \times O3N2, \qquad (2)$$

However, O3N2 calibrations do not consider the variations of the ionization parameter (q), which may cause systematic errors. More will be discussed in the next subsection.

2.5.3. The KK04 Method

Kobulnicky & Kewley (2004, hereafter KK04) adopted the stellar evolution and photoionization from Kewley & Dopita (2002) to produce a modified R_{23} calibration. The R_{23} index, defined as $R_{23} = ([O\ II]\ \lambda3727 + [O\ III]\ \lambda\lambda4959, 5007)/H\beta$, is sensitive to the ionization parameter of the gas, which is defined as the ratio between the number of hydrogen ionizing photons passing through a unit area per second and the hydrogen density of the gas. The ionization parameter is typically derived based on the line ratio $O_{32} = [O\ III]\ \lambda5007/[O\ II]\ \lambda3727$, and it is also sensitive to oxygen abundance; therefore, KK04 applied an iterative process to derive a consistent ionization parameter and oxygen abundance. First, we determined whether the H II regions lie on the upper or lower R_{23} branch with ratio N2O2 = $[N\ II]\ \lambda6583/[O\ II]\ \lambda3727$, then we calculated an initial ionization parameter by assuming a starting oxygen abundance of 8.0 for lower branch and 9.0 for upper branch. The initial ionization parameter is used to calculate an initial oxygen abundance. These processes are iterated until oxygen abundance converges. Errors are generated with the same Monte Carlo algorithm used in direct T_e method, i.e., repeating the calculation 2000 times.

The results of three calibrations, electron temperatures $T[O\ III]$, electron densities n_e, and ionization parameter q are listed in Table 2. To test the reliability of the oxygen abundance, we compare the three calibrations in Figure 5. In Figure 5, we plot O3N2 calibrations and T_e calibrations versus KK04 calibrations, with different colors indicating different ionization parameters (see Figure 5 for details). As shown in this figure, good linear correlations are seen with systematic offsets as a whole. O3N2 calibration is systematically ~0.4 dex lower than KK04 calibration, and it flattens when KK04 calibration is lower than 8.5 due to the limited range of the O3N2 index. T_e calibrations agree well with O3N2 calibrations if we ignore the values near the lower limit of the O3N2 calibration. The systematic biases of different methods are expected, which are investigated by Kewley & Ellison (2008) in detail. The systemic 0.4 dex bias could be caused by temperature fluctuations or gradients within high-metallicity H II regions. In the presence of temperature fluctuations or gradients, [O III] is emitted predominantly in high-temperature zones, where O^{2+} is present only in small amounts. Thus the high electron temperatures estimated from the [O III] $\lambda4363$ line do not reflect the true electron temperature in the H II region, leading to a systematic lower estimation of metallicity by as much as 0.4 dex (Stasińska 2002, 2005; Kewley & Ellison 2008). Moreover, the scattering between O3N2 calibrations and KK04 calibrations is not random. It correlates with ionization parameter q: samples with lower $\log(q)$ tend to have larger measured metallicity. Considering the discussion above, we use KK04 calibrations in the following analysis.

3. Results

3.1. Velocity Field

M101 is a giant and nearly face-on spiral galaxy (Sandage & Tammann 1974; Bosma et al. 1981). The velocity field of M101 has been studied based on the kinematics of HI gas (Bosma et al. 1981) and Hα-data (Comte et al. 1979). In this paper, the H II regions cover a wide range of regions on M101, which enables us to acquire the velocity map for M101. The

left panel of Figure 2 shows the line-of-sight velocities of H II regions in M101, which are good tracers of gas movements. The velocities are measured using the SAO xcsao package with IRAF.

As seen in this panel, a rotating disk is clearly shown. We then apply the harmonic decomposition method (Krajnović et al. 2006) to model the velocity field. This method has been widely used to analyze the gas and stellar kinematics in both late-type (Franx et al. 1994; Wong et al. 2004) and early-type galaxies (Emsellem et al. 2007; Krajnović et al. 2008). This method is able to decompose the line-of-sight velocity map into a series of Fourier components, which are kinematic components with different azimuthal symmetry. In this work, we broadly expand the Fourier terms to the third order:

$$V(a, \psi) = A_0(a) + \sum_{n=1}^{3} A_n(a)\sin n\psi + B_n(a)\cos(n\psi), \quad (3)$$

where ψ is the eccentric anomaly, and a is the length of the semimajor axis of the elliptical ring. Using this model, we obtained the kinematic position angle of 36°, the inclination of 26°, the systemic velocity of 242 km s^{-1} and the line-of-sight rotation velocity of 71 km s^{-1}, corresponding to a maximum rotation velocity of 168 km s^{-1}. These values agree well with the previous modeling of the velocity field from Comte et al. (1979), who found the position angle of 35°, the inclination of 27°, and the systemic velocity of 238 km s^{-1}. However, the inclination measured in this work is slightly larger than the result from Bosma et al. (1981), who found an inclination of 18° based on the HI velocity map. This discrepancy may be due to the larger HI disks than optical disk and interactions with close companions in the outskirts (Bosma et al. 1981; Waller et al. 1997; Mihos et al. 2012). The modeled velocity map is shown in the right panel of Figure 2 with the same color-coding of the left panel.

3.2. Stellar Population Ages

The light-weighted mean stellar age is a good tracer to the star formation history. Low stellar age indicates the young stellar population and recent strong star formation activities in the galaxy, while high stellar age means old stellar populations with few recent star formation activities. The equivalent width (EW) of the Hα emission line is sensitive to the ratio of present to past star formation rates; therefore, it is expected to be correlated with stellar age, and with the higher values of the younger populations.

From the MF-ICA fits, we have estimated the stellar population age by computing the light-weighed mean age of different stellar population components. The left panel of Figure 6 shows the two-dimensional distribution of the mean stellar age. As shown in this figure, the stellar ages of the inner region are generally older than the outskirts in M101. We also present the EW(Hα) of each H II region in the right panel of Figure 6. The results in both of the panels are broadly consistent, with the older stellar population in the inner regions and the younger stellar population in outer regions. This negative stellar age gradient in M101 agrees with the "inside-out" disk growth scenario (Bezanson et al. 2009; Pérez et al. 2013; Tacchella et al. 2015).
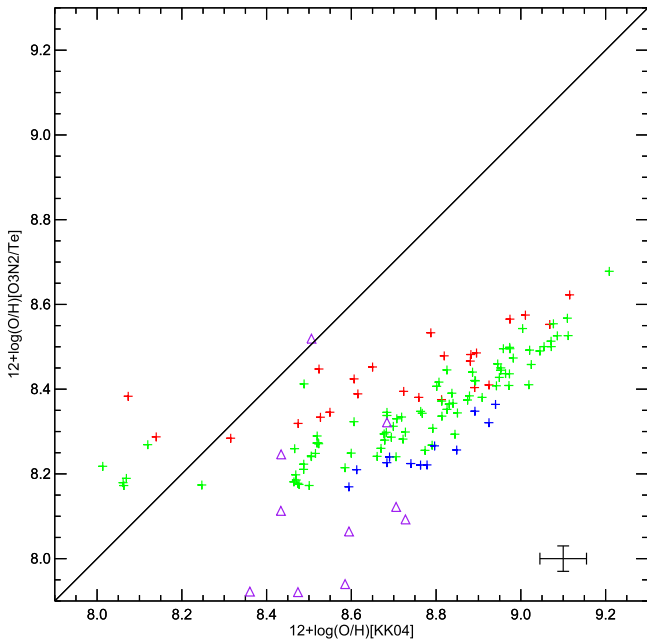
Figure 5. Comparison of the three abundance calibrations. The solid line is the $y = x$ line. Triangle points represent direct T_e calibration, and cross points represent O3N2 calibration. Different colors of cross points indicate different ionization parameters q: red, $\log(q) < 7.2$; green, $7.2 < \log(q) < 7.7$; blue, $\log(q) > 7.7$. The error bar shows the typical error of the measurements.

We note that it appears to have a younger stellar population component at the very center of the bulge (see Figure 6). This is also discovered in Lin et al. (2013) by using SED modelings of resolved multi-band photometric images from ultraviolet and optical to infrared of M101. They found a resolved bar at the center of M101, and proposed that the bulge of M101 is a disk-like pseudobulge, likely induced by secular evolution of the small bar (Hawarden et al. 1986; Ho et al. 1997; Wang et al. 2012; Cole et al. 2014; Lin et al. 2017).

3.3. Radial Abundance Gradient

The measurements of the radial abundance gradient from H II regions are first carried out by Searle (1971) and Smith (1975), after that series of works showed up (McCall et al. 1985; Kennicutt & Garnett 1996; Bresolin 2007; Sánchez et al. 2012a, 2014; Lin et al. 2013; Pilyugin et al. 2014; Sánchez-Menguiano et al. 2016, 2017; Belfiore et al. 2017).

There are 173 out of 188 H II regions whose oxygen abundances are computed by the KK04 calibration. The distribution of oxygen abundance (left panel) and its radial gradient (right panel) are presented in Figure 7. Some other works are also shown with different symbols. As the figure shows, the oxygen abundances from the KK04 calibration are 0.5 dex higher than Bresolin (2007) and Kennicutt et al. (2003), because their calibrations are based on the T_e method. However, the metallicity gradients are consistent based on different calibrations and works. In addition, our result also shows a break in the gradient at around 18 kpc radius, so we use two linear least-squares fits:

$$12 + \log(O/H) = 9.24 - 0.0364 \times R \qquad (4)$$

for $R < 18$ kpc, and

$$12 + \log(O/H) = 8.64 - 0.00686 \times R \qquad (5)$$

for $R > 18$ kpc. The gradient of the inner regions is -0.0364 dex kpc^{-1}, which is slightly steeper than the results from Bresolin (2007), Li et al. (2013), and Pilyugin et al. (2014; -0.0278, -0.0268 and -0.0293 dex kpc^{-1}). However, the metallicity gradient becomes flat at the radius greater than 20 kpc. To compare with the characteristic gradient provided by Ho et al. (2015) (-0.39 ± 0.18 dex R_{25}^{-1}), we convert the derived gradient to the same scale. For inner regions, the gradient is -1.18 ± 0.017 dex R_{25}^{-1}, which is steeper than characteristic gradients. However, the gradient of the outer region is -0.221 ± 0.038 dex R_{25}^{-1}, which is flatter.

Rosales-Ortega et al. (2012) found that gas metallicity increases with stellar mass surface density, which plays a role in determining the mass–metallicity relation and radial metallicity gradients in spirals. This has been confirmed by several researches (e.g., Sánchez et al. 2013; Barrera-Ballesteros et al. 2016). Chemical evolution models with the most important parameters varying smoothly with radius can easily reproduce negative gradients, which show that the maxima of both neutral and molecular gas move from the center to the outskirts through the disk as the galaxy evolves. Thus the star formation is strong in the central regions at early times and spread outward through disks as the gas is efficiently consumed. This shapes present galaxies with high-metallicity, low specific star formation rate in the center and negative radial metallicity gradients that flatten with time. This is known as the "inside-out" disk growth.

Several studies have found that metallicity gradients flatten to a constant value beyond the isophotal radii R_{25} or $2R_e$ (Rosales-Ortega et al. 2011; Marino et al. 2012; Sánchez et al. 2012b, 2014; López-Sánchez et al. 2015; Sánchez-Menguiano et al. 2016). The mechanism of this gradient flattening is under debate. One possible mechanism is a slow radial dependence of the star formation efficiency across large galactocentric distances (Bresolin et al. 2012; Esteban et al. 2013). Cosmological simulations that introduce a balance between outflows and inflows with the intergalactic medium may also contribute to shaping the metal content (Oppenheimer & Davé 2008; Oppenheimer et al. 2010; Davé et al. 2011, 2012). Interactions with satellite galaxies are suggested to enhance the metallicity in the outer regions of galaxies, which may also flatten the metallicity gradient (Bird et al. 2012; López-Sánchez et al. 2015). The real senario is likely to be the mixture of several mechanisms. We note that the turning point of the gradient in M101 is at ~18 kpc, which is much smaller than $R_{25}(\sim31$ kpc). An alternative explanation is proposed by Lépine et al. (2011), who state that the break in the gradient is the "pumping out" effect of corotation, which produces gas flows in opposite directions on the two sides of the radius. The corotation radius of M101 is 16.7 kpc (Scarano & Lépine 2013), which is very close to the break radius we find in this work. This suggests that the radial break of metallicity in M101 is probably caused by the result of corotation.

There are seven outliers far below the fit line with oxygen abundances lower than 8.2. These H II regions are located to the east of M101. M101 is not the isolated galaxy, and two close companions (NGC 5474 in the east and NGC 5477 in the southeast) are found. Kewley et al. (2006) presented some evidence that galaxy pairs have systematically lower oxygen abundance than field galaxies, and mergers may also flatten the oxygen abundance gradient. More recently, Sánchez et al.
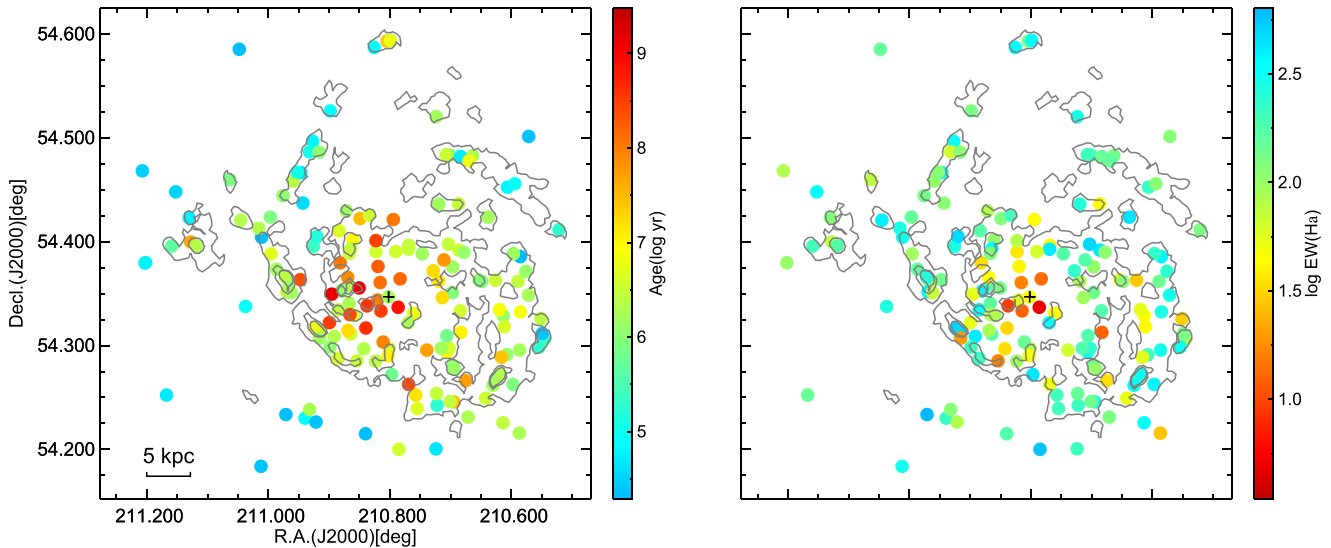
Figure 6. Two-dimensional distribution of stellar population age and EW(Hα). Contours show the shape of M101 in the Hα image, and the center of the galaxy is marked with a black cross.
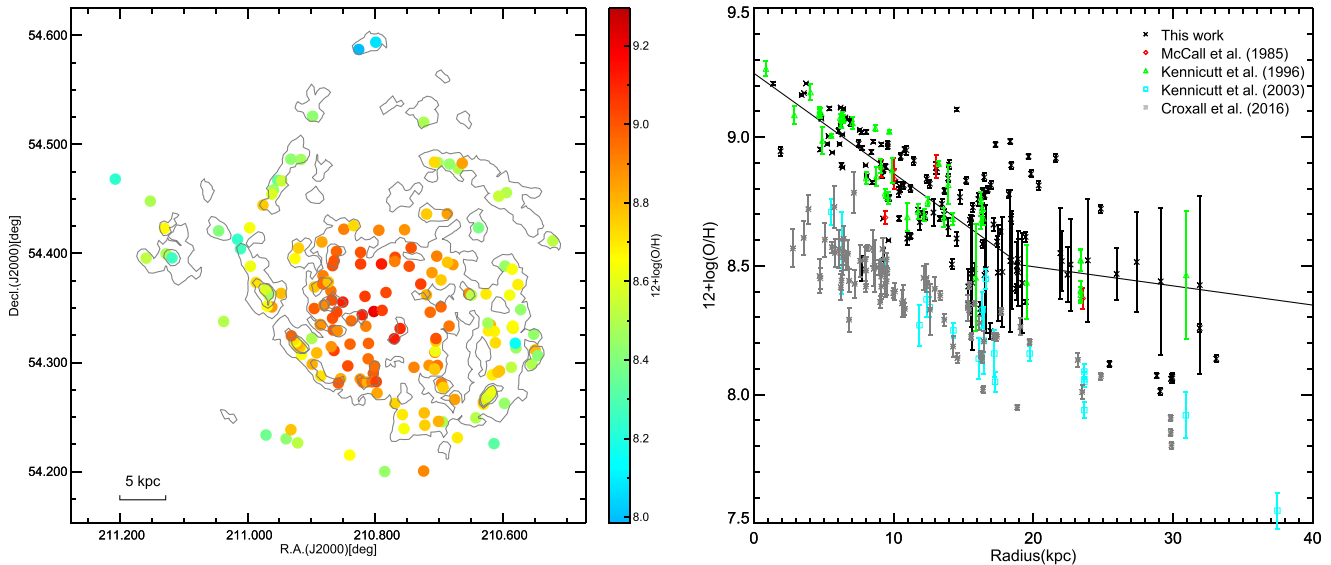
Figure 7. Left: distributions of metallicities of H II regions in M101. Right: radial metallicity gradient for H II regions. Metallicities are determined from KKO4 calibration for this plot.

(2014) found that the metallicity gradients are independent of morphology, incidence of bars, absolute magnitude, and mass, and that the only clear correlation is between merger stage and metallicity gradient, where merger progresses flatten the slope of gradients (see also Kewley et al. 2010; Rupke et al. 2010; Rich et al. 2012; Torrey et al. 2012). M101 might be interacting with NGC5 474 and NGC 5477, as suggested by Waller et al. (1997) and Mihos et al. (2012, 2013), who analyzed deep neutral hydrogen observation and deep optical images and concluded that M101 is in an ongoing interaction with lower mass companions. These interactions may dilute the oxygen abundance of these H II regions in gas mixing processes, making the seven outliers relatively meta-poor.

4. Summary

We have investigated the distributions of physical properties of H II regions in the nearby galaxy M101 using spectra obtained from the 6.5 m MMT telescope and the NAOC 2.16 m telescope during 2012–2014. We present the observations, data reductions, and measurements of emission lines. This is the largest spectroscopic sample of H II regions in M101 by now.

We estimated the stellar population ages by fitting the continuum with the MF-ICA approach, and the stellar age profile shows an older stellar population in the inner regions and a younger in the outer regions. There is a younger component at the center of the galaxy, which indicates that recent star formation occurred at the center. This might be caused by gas falling into the center due to the nonaxisymmetric gravity of the bar.

We calculated the electron temperatures T[O III], electron densities n_e, and measured oxygen abundances with three methods. O3N2 calibrations are consistent with direct T_e calibrations when we ignore the limitation effect of O3N2 calibration, and both calibrations are systemically ∼0.4 dex

lower than the KK04 calibration, due to temperature fluctuations or gradients within high-metallicity H II regions. O3N2 calibrations do not consider ionization parameters, which may cause systemic errors.

The oxygen abundance profile shows a negative gradient with a clear break at 20 kpc radius. The gradient is $-0.0364\,\mathrm{dex\,kpc^{-1}}$ in the inner region and $-0.00686\,\mathrm{dex\,kpc^{-1}}$ in the outer region. This is likely to be the mixture of several mechanisms, such as radial dependence of SFE over large galactocentric distances, a balance between outflows and inflows with the intergalactic medium and interactions with satellite galaxies. Since the break radius is comparable to the corotation radius (16.7 kpc), the break in the gradient could be the "pumping out" effect of corotation. If this is the case, gas flows play an important role in chemical evolutions of galaxies and should not be regarded as minor effects in evolution models. There are several H II regions with oxygen abundances lower than 8.2, which are located far from the major distribution, and we find that they are all located to the east of M101, close to its companions, NGC 5474 and NGC 5477. These low metallicities may be the result of interactions with close companions.

Both stellar population age distribution and oxygen abundance gradient support the "inside-out" disk growth scenario: the early gas infall or collapse made the inner region more metal-rich and older, while the outer disk is enriched more slowly and younger. In order to learn more about the formation and evolution of nearby galaxies, we intend to combine the spectra of H II regions with multi-wavelength photometry data (especially UV to IR) to investigate the nature of dispersions of the IRX-β relation. Due to the relatively simple star formation history and structure of H II regions, it would be helpful to find a second parameter to reduce the scatter of IRX-β relation. This will help us to further understand the interaction between dust and the interstellar radiation field, as well as the formation and evolution of nearby galaxies.

Facilities: MMT, Beijing:2.16m.

Software: SExtractor (Bertin & Arnouts 1996), xfitfibs, HSRED, MF-ICA (Hu et al. 2016), MPFIT (Markwardt 2009), PyNeb (Luridiana et al. 2015).

ORCID iDs

Ning Hu ⬤ https://orcid.org/0000-0002-2941-734X
Enci Wang ⬤ https://orcid.org/0000-0003-1588-9394
Zesen Lin ⬤ https://orcid.org/0000-0001-8078-3428
Xu Kong ⬤ https://orcid.org/0000-0002-7660-2273
Jing Wang ⬤ https://orcid.org/0000-0002-6880-4481
Hu Zou ⬤ https://orcid.org/0000-0002-6684-3997

References

Aggarwal, K. M., & Keenan, F. P. 1999, ApJS, 123, 311
Alloin, D., Collin-Souffrin, S., Joly, M., & Vigroux, L. 1979, A&A, 78, 200
Bacon, R., Copin, Y., Monnet, G., et al. 2001, MNRAS, 326, 23
Baldwin, J. A., Phillips, M. M., & Terlevich, R. 1981, PASP, 93, 5
Barrera-Ballesteros, J. K., Heckman, T. M., Zhu, G. B., et al. 2016, MNRAS, 463, 2513
Belfiore, F., Maiolino, R., Tremonti, C., et al. 2017, MNRAS, 469, 151
Berg, D. A., Skillman, E. D., Garnett, D. R., et al. 2013, ApJ, 775, 128
Bertin, E., & Arnouts, S. 1996, A&AS, 117, 393
Bezanson, R., van Dokkum, P. G., Tal, T., et al. 2009, ApJ, 697, 1290
Bird, J. C., Kazantzidis, S., & Weinberg, D. H. 2012, MNRAS, 420, 913
Bosma, A., Goss, W. M., & Allen, R. J. 1981, A&A, 93, 106
Bresolin, F. 2007, ApJ, 656, 186
Bresolin, F., Kennicutt, R. C., & Ryan-Weber, E. 2012, ApJ, 750, 122
Bruzual, G., & Charlot, S. 2003, MNRAS, 344, 1000
Bundy, K., Bershady, M. A., Law, D. R., et al. 2015, ApJ, 798, 7
Cardelli, J. A., Clayton, G. C., & Mathis, J. S. 1989, ApJ, 345, 245
Cavichia, O., Mollá, M., Costa, R. D. D., & Maciel, W. J. 2014, MNRAS, 437, 3688
Charlot, S., & Fall, S. M. 2000, ApJ, 539, 718
Chiappini, C., Matteucci, F., & Romano, D. 2001, ApJ, 554, 1044
Cole, D. R., Debattista, V. P., Erwin, P., Earp, S. W. F., & Roškar, R. 2014, MNRAS, 445, 3352
Comte, G., Monnet, G., & Rosado, M. 1979, A&A, 72, 73
Croxall, K. V., Pogge, R. W., Berg, D. A., Skillman, E. D., & Moustakas, J. 2016, ApJ, 830, 4
Cutri, R. M., Skrutskie, M. F., van Dyk, S., et al. 2003, yCat, 2246, 1
Dalcanton, J. J., Yoachim, P., & Bernstein, R. A. 2004, ApJ, 608, 189
Davé, R., Finlator, K., & Oppenheimer, B. D. 2011, MNRAS, 416, 1354
Davé, R., Finlator, K., & Oppenheimer, B. D. 2012, MNRAS, 421, 98
De Robertis, M. M., Dufour, R. J., & Hunt, R. W. 1987, JRASC, 81, 195
Emsellem, E., Cappellari, M., Krajnović, D., et al. 2007, MNRAS, 379, 401
Esteban, C., Carigi, L., Copetti, M. V. F., et al. 2013, MNRAS, 433, 382
Fabricant, D., Fata, R., Roll, J., et al. 2005, PASP, 117, 1411
Fan, Z., Wang, H., Jiang, X., et al. 2016, PASP, 128, 5005
Franx, M., van Gorkom, J. H., & de Zeeuw, T. 1994, ApJ, 436, 642
Fu, J., Hou, J.-L., Yin, J., & Chang, R. X. 2009, ApJ, 696, 668
Garnett, D. R. 1992, AJ, 103, 1330
Gordon, K. D., Engelbracht, C. W., Rieke, G. H., et al. 2008, ApJ, 682, 336
Hawarden, T. G., Mountain, C. M., Leggett, S. K., & Puxley, P. J. 1986, MNRAS, 221, 41
Ho, I.-T., Kudritzki, R.-P., Kewley, L. J., et al. 2015, MNRAS, 448, 2030
Ho, L. C., Filippenko, A. V., & Sargent, W. L. W. 1997, ApJ, 487, 591
Hodge, P. W., Gurwell, M., Goldader, J. D., & Kennicutt, R. C., Jr. 1990, ApJS, 73, 661
Højen-Sørensen, P. A. D. F. R., Winther, O., & Hansen, L. K. 2001, Advances in Neural Information Processing Systems, Vol. 13 (Cambridge, MA: MIT Press)
Højen-Sørensen, P. A. D. F. R., Winther, O., & Hansen, L. K. 2002, Neural Comput, 14, 889
Hoopes, C. G., Walterbos, R. A. M., & Bothun, G. D. 2001, ApJ, 559, 878
Hu, N., Su, S.-S., & Kong, X. 2016, RAA, 16, 42
Kauffmann, G., Heckman, T. M., Tremonti, C., et al. 2003, MNRAS, 346, 1055
Kennicutt, R. C., Jr., Bresolin, F., & Garnett, D. R. 2003, ApJ, 591, 801
Kennicutt, R. C., Jr., & Garnett, D. R. 1996, ApJ, 456, 504
Kewley, L. J., & Dopita, M. A. 2002, ApJS, 142, 35
Kewley, L. J., Dopita, M. A., Sutherland, R. S., Heisler, C. A., & Trevena, J. 2001, ApJ, 556, 121
Kewley, L. J., & Ellison, S. L. 2008, ApJ, 681, 1183
Kewley, L. J., Geller, M. J., & Barton, E. J. 2006, AJ, 131, 2004
Kewley, L. J., Rupke, D., Zahid, H. J., Geller, M. J., & Barton, E. J. 2010, ApJL, 721, L48
Kobulnicky, H. A., & Kewley, L. J. 2004, ApJ, 617, 240
Kong, X., Lin, L., Li, J.-r., et al. 2014, ChA&A, 38, 427
Krajnović, D., Bacon, R., Cappellari, M., et al. 2008, MNRAS, 390, 93
Krajnović, D., Cappellari, M., de Zeeuw, P. T., & Copin, Y. 2006, MNRAS, 366, 787
Lépine, J. R. D., Cruz, P., Scarano, S., Jr., et al. 2011, MNRAS, 417, 698
Li, Y., Bresolin, F., & Kennicutt, R. C., Jr. 2013, ApJ, 766, 17
Lin, L., Li, C., He, Y., Xiao, T., & Wang, E. 2017, ApJ, 838, 105
Lin, L., Zou, H., Kong, X., et al. 2013, ApJ, 769, 127
López-Sánchez, Á R., Westmeier, T., Esteban, C., & Koribalski, B. S. 2015, MNRAS, 450, 3381

Luridiana, V., Morisset, C., & Shaw, R. A. 2015, A&A, 573, A42
Marino, R. A., Gil de Paz, A., Castillo-Morales, A., et al. 2012, ApJ, 754, 61
Marino, R. A., Rosales-Ortega, F. F., Sánchez, S. F., et al. 2013, A&A, 559, A114
Markwardt, C. B. 2009, in ASP Conf. Ser. 411, Astronomical Data Analysis Softwar and Systems XVIII, ed. D. A. Bohlender, D. Durand, & P. Dowler (San Francisco, CA: ASP), 251
Massey, P., Strobel, K., Barnes, J. V., & Anderson, E. 1988, ApJ, 328, 315
McCall, M. L., Rybski, P. M., & Shields, G. A. 1985, ApJS, 57, 1
Mihos, J. C., Harding, P., Spengler, C. E., Rudick, C. S., & Feldmeier, J. J. 2013, ApJ, 762, 82
Mihos, J. C., Keating, K. M., Holley-Bockelmann, K., Pisano, D. J., & Kassim, N. E. 2012, ApJ, 761, 186
Oppenheimer, B. D., & Davé, R. 2008, MNRAS, 387, 577
Oppenheimer, B. D., Davé, R., Kereš, D., et al. 2010, MNRAS, 406, 2325
Pérez, E., Cid Fernandes, R., González Delgado, R. M., et al. 2013, ApJL, 764, L1
Pettini, M., & Pagel, B. E. J. 2004, MNRAS, 348, L59
Pilyugin, L. S. 2003, A&A, 397, 109
Pilyugin, L. S., Grebel, E. K., & Kniazev, A. Y. 2014, AJ, 147, 131
Podobedova, L. I., Kelleher, D. E., & Wiese, W. L. 2009, JPCRD, 38, 171
Rich, J. A., Torrey, P., Kewley, L. J., Dopita, M. A., & Rupke, D. S. N. 2012, ApJ, 753, 5
Rosales-Ortega, F. F., Díaz, A. I., Kennicutt, R. C., & Sánchez, S. F. 2011, MNRAS, 415, 2439
Rosales-Ortega, F. F., Kennicutt, R. C., Sánchez, S. F., et al. 2010, MNRAS, 405, 735
Rosales-Ortega, F. F., Sánchez, S. F., Iglesias-Páramo, J., et al. 2012, ApJL, 756, L31
Roy, J.-R., & Walsh, J. R. 1997, MNRAS, 288, 715
Rupke, D. S. N., Kewley, L. J., & Barnes, J. E. 2010, ApJL, 710, L156
Sánchez, S. F., Kennicutt, R. C., Gil de Paz, A., et al. 2012a, A&A, 538, A8
Sánchez, S. F., Pérez, E., Rosales-Ortega, F. F., et al. 2015, A&A, 574, A47
Sánchez, S. F., Rosales-Ortega, F. F., Iglesias-Páramo, J., et al. 2014, A&A, 563, A49
Sánchez, S. F., Rosales-Ortega, F. F., Jungwiert, B., et al. 2013, A&A, 554, A58
Sánchez, S. F., Rosales-Ortega, F. F., Marino, R. A., et al. 2012b, A&A, 546, A2
Sánchez-Menguiano, L., Sánchez, S. F., Pérez, I., et al. 2016, A&A, 587, A70
Sánchez-Menguiano, L., Sánchez, S. F., Pérez, I., et al. 2017, A&A, 603, A113
Sandage, A., & Tammann, G. A. 1974, ApJ, 194, 223
Scarano, S., & Lépine, J. R. D. 2013, MNRAS, 428, 625
Schlegel, D. J., Finkbeiner, D. P., & Davis, M. 1998, ApJ, 500, 525
Searle, L. 1971, ApJ, 168, 327
Shaw, R. A., & Dufour, R. J. 1995, PASP, 107, 896
Smith, H. E. 1975, ApJ, 199, 591
Stasińska, G. 2002, RMxAC, 12, 62
Stasińska, G. 2005, A&A, 434, 507
Storey, P. J., & Zeippen, C. J. 2000, MNRAS, 312, 813
Tacchella, S., Carollo, C. M., Renzini, A., et al. 2015, Sci, 348, 314
Tayal, S. S., & Zatsarinny, O. 2010, ApJS, 188, 32
Torrey, P., Cox, T. J., Kewley, L., & Hernquist, L. 2012, ApJ, 746, 108
Tremonti, C. A., Heckman, T. M., Kauffmann, G., et al. 2004, ApJ, 613, 898
Trujillo, I., Förster Schreiber, N. M., Rudnick, G., et al. 2006, ApJ, 650, 18
van Zee, L., Salzer, J. J., Haynes, M. P., O'Donoghue, A. A., & Balonek, T. J. 1998, AJ, 116, 2805
Waller, W. H., Bohlin, R. C., Cornett, R. H., et al. 1997, ApJ, 481, 169
Wang, Y., Zhao, H., Mao, S., & Rich, R. M. 2012, MNRAS, 427, 1429
Wiese, W. L., Fuhr, J. R., & Deters, T. M 1996, Atomic Transition Probabilities of Carbon, Nitrogen, and Oxygen: a Critical Data Compilation (Melville, NY: AIP)
Wong, T., Blitz, L., & Bosma, A. 2004, ApJ, 605, 183
Zaritsky, D. 1992, ApJL, 390, L73
Zaritsky, D., Kennicutt, R. C., Jr., & Huchra, J. P. 1994, ApJ, 420, 87